

We are IntechOpen, the world's leading publisher of Open Access books Built by scientists, for scientists

6,900

Open access books available

185,000

International authors and editors

200M

Downloads

Our authors are among the

154

Countries delivered to

TOP 1%

most cited scientists

12.2%

Contributors from top 500 universities



WEB OF SCIENCE™

Selection of our books indexed in the Book Citation Index
in Web of Science™ Core Collection (BKCI)

Interested in publishing with us?
Contact book.department@intechopen.com

Numbers displayed above are based on latest data collected.
For more information visit www.intechopen.com



Characterization of Microdevices by Nanoindentation

Mamadou Diobet DIOP

Additional information is available at the end of the chapter

<http://dx.doi.org/10.5772/50997>

1. Introduction

In the last two decades, the study of microdevices such as micro-electro-mechanical systems (MEMS) has rapidly grown into a critical area of technology with several applications that impact many industrial sectors including automotive, consumer electronics, telecommunication, aerospace, and medical.

Microdevices can undergo early failure during the operation due to mechanical stresses, which can be induced by a single high stress or cyclic low stresses compared with the strength of the component. An accurate knowledge of the mechanical properties of micro and nanomaterials, especially thin films, which form mechanical structures of MEMS systems, is necessary to minimize or virtually eliminate failures. Mechanical properties of bulk materials were widely investigated as compared to thin films. In many cases, thin films properties differ from that of the bulk materials owing to the presence of residual stresses, preferred orientations of crystallographic planes, and the morphology of the microstructure [1, 2]. The studies of thin films properties were mostly done for the semiconductor industry, but they were mainly on the electrical properties [2]. Usually, when the mechanical properties of micro and nanomaterials are studied, thin continuous films deposited on a silicon wafer are used. This differs to patterned thin film deposited on structures of microdevices where film exists as individual part with different shapes and various cross-section geometries. Contrary to the continuous films use case, the deformation field in the line structure is dominated by the edge effect [3]. So, extracting the realistic behavior of materials for preventing failures dictates a direct mechanical characterization of the thin film structures in a configuration similar to the actual microdevices final design.

This chapter is centered around presenting the mechanical characterization of such microdevices using nanoindentation technique. These microdevices studied here are not limited to MEMS structures but also include micropillars and cylindrical bumps used in flip

chip technology. Nanoindentation has been used so far to locally extract the Young's modulus and the hardness of materials. Here, we present the extension of this technique to characterize the microdevices structures. Beyond the high resolutions in load and displacement, nanoindentation offers the possibility to vertically load the structures similarly to their actual functioning in the components. The main experimental difficulty in characterizing the microdevices by nanoindentation is to ensure that the measured load-deflection data reflect the true deformation of the sample under test. We have intentionally based this study mainly on the experimental challenges; theoretical analysis is given for understanding of the evaluation of the mechanical properties.

For MEMS structures study, the conventional nanoindentation is used without any modification, as reported in the first section, with the intention of determining the elastic and plastic constants as well as the fatigue strength of cantilever and bridge microbeams. The second section is devoted to the uniaxial compression of micropillars in order to investigate the size effects on their plastic flow. The last section presents a study of the insertion of cylindrical bumps for flip-chip interconnection applications. To achieve this goal, major modifications related to sample holders both on the nanoindenter column extremity and the stage, are performed. The reliability of MEMS structures and the cylindrical bumps require both mechanical and electrical studies. So, electrical measurements can be synchronized with the nanoindenter in order to couple the mechanical and electrical mechanisms.

2. MEMS characterization by nanoindentation

The International Technology Roadmap for Semiconductors (ITRS), 2011 edition described MEMS as devices that are composed of micrometer-sized mechanical structures (suspended bridges, cantilevers, membranes, fluid channels, etc.) and often integrated with analog and digital circuitry. MEMS can act as sensors, receiving information from their environment, or as actuators, responding to a decision from the control system to change the environment. The majority of today's MEMS products include accelerometers, pressure and chemical flow sensors, micromirrors, gyroscopes, fluid pumps, and inkjet print heads. All MEMS sectors such automotive, optical MEMS, magnetometers for consumers and industrial high-end applications exceeded growth expectations in 2010. To sustain an annual market growth, the development of new innovative MEMS must be pursued and great efforts must be dedicated to reliability issues. In this section we focus on the mechanical reliability of micromaterials for MEMS structures as it is the principle part of the MEMS reliability [2].

Several reliability test methods have been employed in MEMS and they all differ depending on the user interest. Mechanical testing of MEMS using nanoindentation is related to the bending tests of samples such cantilever and bridge beams. The purpose being to extract the elastic and plastic characteristics as well as the failure mechanism of the mobile parts of the MEMS.

2.1. Specimen manufacturing

The common MEMS processes named surface manufacturing and bulk manufacturing are mostly employed to build the mobile parts of MEMS structures (cantilever and bridges microbeams). These two manufacturing techniques use processing steps that are compatible with the silicon Integrated Circuits (ICs) technology. The surface micromachining uses two thin layers—a structural material (polysilicon, Al, SiO₂, ...) and a sacrificial material (SiO₂, polymers, Al, ...) deposited on the surface of a silicon substrate to fabricate the mobile parts of the MEMS. The bulk micromachining technique employs the whole thickness of a silicon wafer to build the micro-mechanical structures [4]. In bulk micromachining, the air gap underneath the mobile parts are limited by the silicon thickness (up to 530 μm for a standard wafer) while the surface micromachining leads to small air gap defined by the sacrificial layer which is less than 1.5 μm thick [4]. Deep gap air allows large deformations during mechanical bending; this explains the wide use of nanoindentation for MEMS structures made by bulk micromachining compared to those obtained by surface micromachining.

2.2. Bending test by nanoindentation

Two experimental configurations of the bending test are presented here: bending of cantilever and bridge microbeams. As in the conventional nanoindenter, the recorded load-displacement data are used to determine the mechanical properties of the cantilever and the bridge microbeams through theoretical models. However the model employed in the bending tests is different to the standard Oliver and Pharr model [5].

2.2.1. Bending test of single-layer cantilever

The principle of the mechanical bending of cantilever microbeams by nanoindentation was firstly introduced in [6]. The test was done by applying a load with the nanoindenter tip at the edge of the free extremity of the cantilever while the load-deflection was continuously recorded. The principle of the bending test is shown in Figure 1; where e , l and L are the thickness, the width and the length of the cantilever, respectively. The dimensions of the structures in MEMS devices have wide ranges, from submicrometers to millimeters. Thus, evaluations of the mechanical properties of thin films cover a very wide range of measurement scale.

-Young modulus

According to the beam bending theory, the relationship between the Young's modulus, E , the cantilever geometry, the deflection, δ , at an arbitrary point "B" and the contacting load, P , is described as follow [7]:

$$E = \frac{P}{\delta} \frac{4(1-\nu^2)L^3}{le^3} \quad (1)$$

where ν is the Poisson's ratio of the cantilever material. E is obtained by extracting the initial linear slope, P/δ , from the load-deflection curve recorded by the nanoindenter [6, 8, 9]. An example of a load-deflection curve is seen in Figure 2. The above relation is applicable only for small beam deflections ($\delta \ll L$).

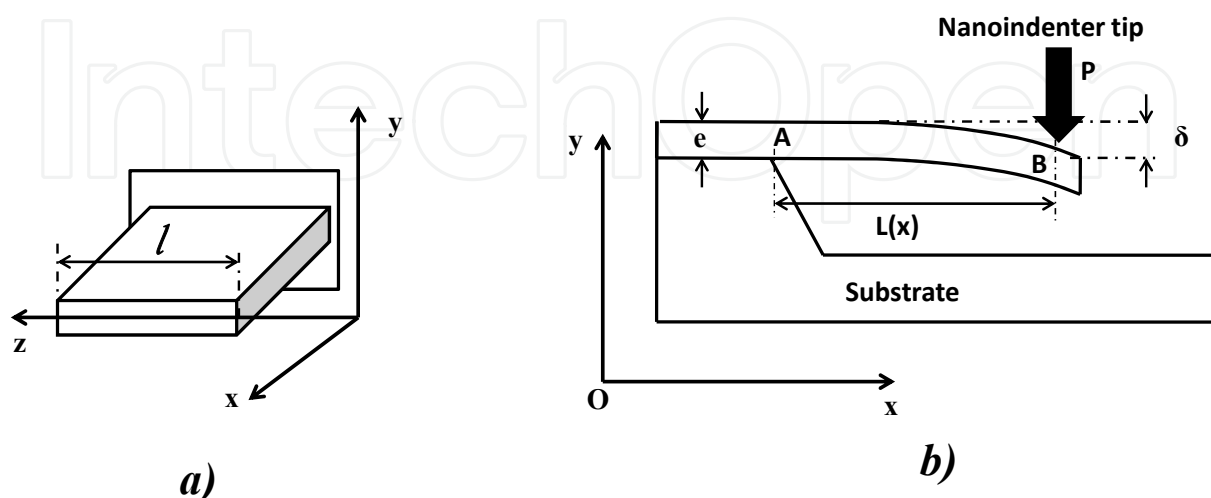


Figure 1. a) Cantilever geometry and b) principle of the bending test of cantilever beam by nanoindentation.

-Yield strength

Another interesting parameter to be extracted by bending test is the yielding strength of the cantilever material. This is obtained using the stress formula in the cantilever which reaches its maximum value at the fixed end of the beam where the applied moment is greatest (point "A" in Figure 1b). When this maximum stress reaches the yield strength of the material, the cantilever begins to deform plastically. This permanent deformation can be recognized in the plot of load-deflection curve by a deviation from linearity (Figure 2). The load at this deviation is noted the yield load, P_y , and the yield strength is given by [8]:

$$\sigma_y = \frac{6P_y L}{le^2} \quad (2)$$

The Table 1 summarizes the Young's modulus and the yield strength obtained after bending tests of Al and Au materials [8]. In parallel, standard nanoindentation was carried out on the same samples in order to verify the bending tests results. The comparison between Young's modulus obtained with the two methods show close agreements with errors within 5%. For the yield strength, the values obtained by the authors are much higher than the bulk values. This fact is not surprising because of the dependency of the plastic behavior of thin films with microstructure morphology and residual stresses. These studies have proven that the cantilever bending by nanoindentation can be used to accurately measure the mechanical properties of thin films.

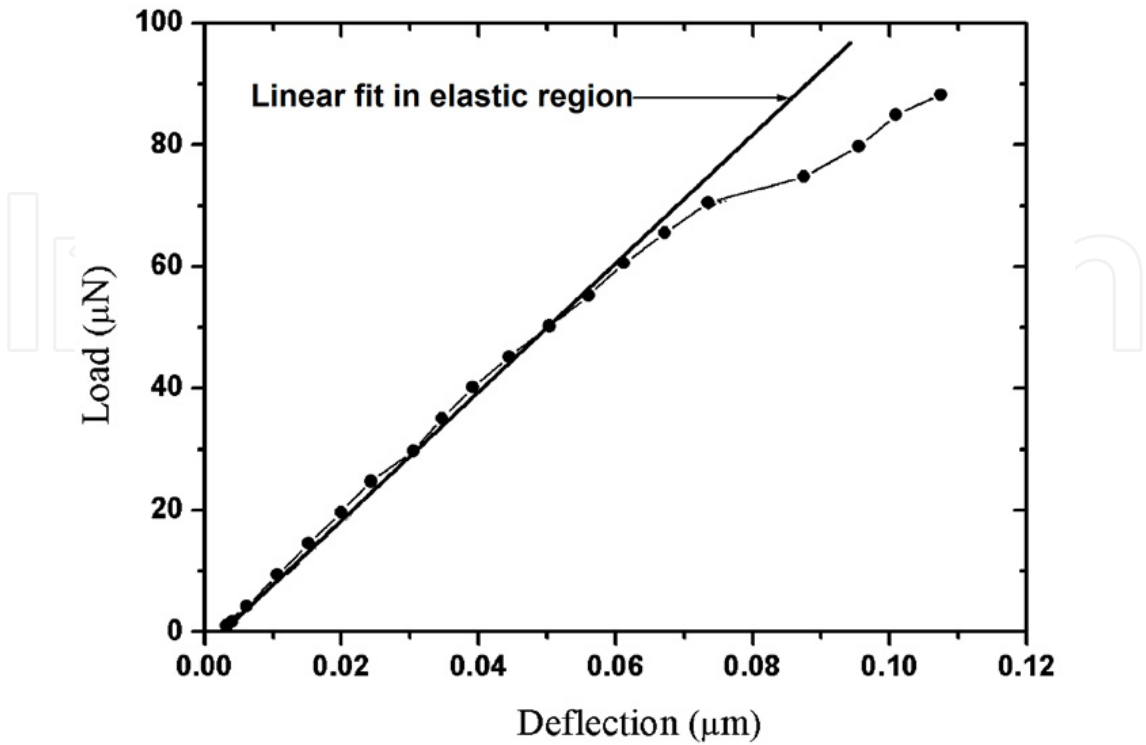


Figure 2. Load versus deflection of an Al cantilever in elastic-plastic region by nanoindentation technique [8].

Film	Thickness (μm)	Young's modulus (GPa)		Yield strength (MPa)
		Cantilever beam	Nanoindentation	Cantilever beam
Al	0.51	80.9	79.3	200.1
	1.03	79.6	73.7	135.7
	1.5	77.6	74.3	114.3
Au	0.56	130.3	122.7	391.4
	0.99	108.7	112.5	309.9
	1.26	107.2	110.4	114.7

Table 1. Experimentally Young's modulus and yield strength of Al and Au films [8].

2.2.2. *Bending test of single-layer bridge microbeam*

Young's modulus and bending strength can be measured by nanoindentation for a fixed bridge microbeam loaded at its center (Figure 3a). For bridge beams that follow linear elastic

theory of an isotropic material, the Young's modulus under given load can be expressed as [10]

$$E = \frac{l^3}{192I} \frac{P}{\delta} \quad (3)$$

where l is the beam length, I is the area moment of inertia for the beam cross-section and P/δ is the slope of the load–deflection curve during bending. The area moment of inertia is calculated from the following equation [10]:

$$I = \frac{w_1^2 + 4w_1w_2 + w_2^2}{36(w_1 + w_2)} t^3 \quad (4)$$

where w_1 and w_2 are the upper and lower widths, respectively, and t is the thickness of the beam.

The bending strength, σ_b , corresponds to the maximum tensile stress which is produced on the top surface at the two ends and it is given by [10]:

$$\sigma_b = \frac{P_{\max} l e_1}{8I} \quad (5)$$

where P_{\max} is the applied load at the failure and e_1 is the distance of the top surface from the neutral plane of the beam cross-section and is given by [10]:

$$e_1 = \frac{t(w_1 + 2w_2)}{3(w_1 + w_2)} \quad (6)$$

An example of a linear loading followed by an abrupt failure of a Si nanobeam bent for failure analysis is presented in Figure 3b [11].

2.3. Fatigue behavior

Fatigue tests of MEMS are also of interest especially for the MEMS involving vibrating structures such as oscillators, vibratory gyroscopes [12], comb drive actuators [2] and hinges in digital micromirror devices (DMD) [13]. For example of DMD, the mirror in normal operating mode switches once every 200 microseconds for 5 years at 1000 operating hours per year. This means each mirror element needed to rotate, or switch, more than 90×10^9 times to ensure a reliable MEMS product [13]. Fatigue tests have been presented in [11] where nanobeams were deformed with cyclic stresses using a nanoindenter through the “continuous stiffness measurement” (CSM) method; in which stiffness is measured continuously during the loading. The CSM technique has been described in detail in reference [5]. In reference [11], the fatigue behavior of Si nanobeams was characterized by monitoring the change in contact stiffness versus the number of cycles as shown in Figure 3c. Fatigue damage was determined by the sudden decrease in contact stiffness which occurred for the Si nanobeams at 0.6×10^4 cycles.

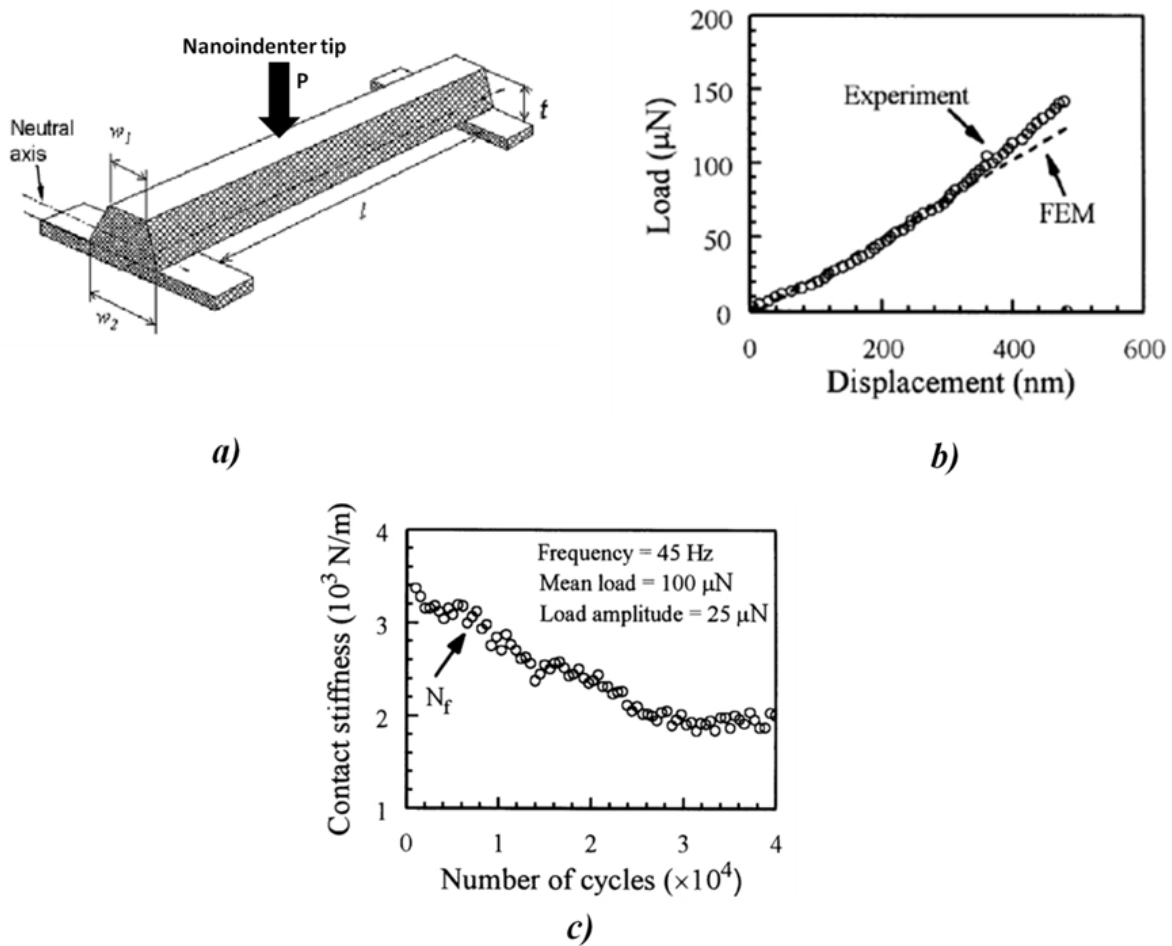


Figure 3. a) A schematic of a typical nanobeam under central loading, b) Load–displacement curve of a Si nanobeam obtained from a nanoindentation experiment, and c) Contact stiffness as a function of the number of cycles for a Si nanobeam cyclically deformed by an oscillation load amplitude of 25 mN with a mean load of 100 mN at a frequency of 45 Hz [11].

2.4. MEMS switches microcontacts characterization by nanoindentation

MEMS switches are switching device that are fabricated using the micromachining technology, where the switching between the on- and off-states is achieved via a pair of microcontacts. One microcontact is typically rigid in space and the other microcontact is movable since it is a part of the deformable elastic structure of the switch. The displacement is induced by various actuation mechanisms such as electrostatic, electrothermal, magnetostatic, and electromagnetic. So, the reliability of MEMS switches depends on both the mechanical and the electrical aspects and the main failure of switches occurs in the microcontacts. Therefore, a realistic characterization of MEMS switches requires a simultaneous study of the mechanical and electrical aspects. To achieve this goal, a nanoindenter is combined and synchronized with an electrical resistance measurement technique (see Figure 4). The nanoindenter controls the movement of the deformable structure and also records the load-displacement or the contact stiffness data while the electrical apparatus measures the variations of the electrical resistance of the microcontacts.

Typical contact loads used in MEMS switches range from a few μN to several hundred μN [14].

An example of the evolution of the contact stiffness and the contact resistance versus applied load for a $175\mu\text{m}$ long Au cantilever is presented in Figure 5 [15]. The main result that can be deduced from the Figure 5 is that the electrical contact was not simultaneously established with the mechanical actuation of the switch. A gap of $20\mu\text{N}$ is noticed and can be explained by the analysis of the contact interface between the two contacting materials. Contact between two bodies occurs at discrete spots produced by the mechanical contact asperities of the two surfaces.

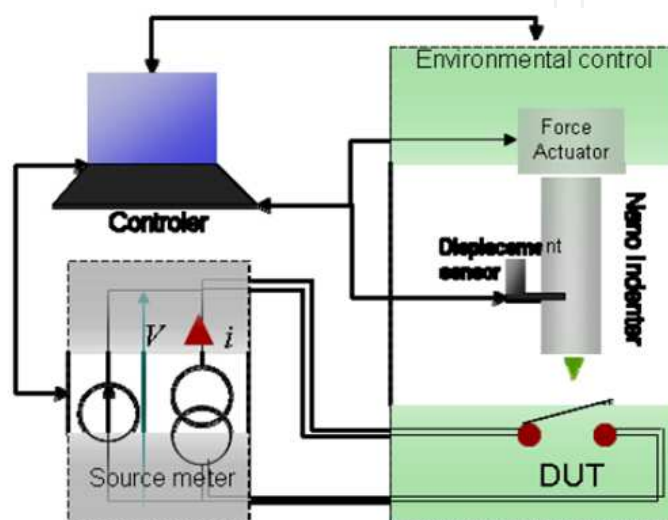


Figure 4. Principle of mechanical and electrical tests of MEMS switches by nanoindentation [9].

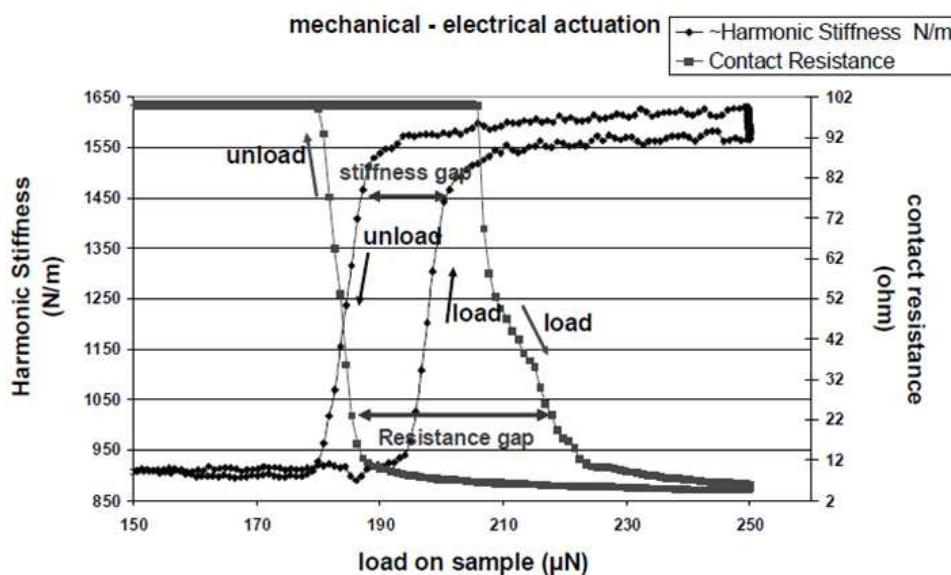


Figure 5. Stiffness and contact resistance versus applied load [15].

This true contact area is smaller than the nominal contact area, leading to high resistance values at the first stage of the actuation.

The calculation of the contact resistance between two bodies is usually done by using the Holm's electric contact theory [16]. In this theory, the contact resistance, R_c , between two contacting bodies of resistivity ρ is equal to:

$$R_c = \frac{\rho}{2a} \quad (7)$$

where a is the radius of the contact area which is assumed to be a unique circular spot. However, this model is not realistic because it does not take into account the multiple contact spots within the area of contact due to both the large-scale waviness and the surface roughness of the contacting materials. Other assumptions of the Holm's theory are related on the fact that the contacting bodies are considered as semi-infinite compared to the area of contact and the surface contamination on the contacts such as oxide film is ignored. The radius of the contact area is linked to the mechanical parameters such as the applied load, P , and the hardness, H , of the softer material and it is expressed as follow [16]:

$$a = \sqrt{\frac{P}{\pi H}} \quad (8)$$

Failure analysis such adhesion of the microcontacts can also be investigated by measuring the contact resistance variation over a mechanical cycling of the switch [17]. For a rounded microcontact bump coated with 300 nm of gold studied in [17], the adhesion failure was noticed after 60,000 contact cycles. This is illustrated by significant changes in pull-off force and contact stiffness (Figure 6a). Also, the adhesion failure is illustrated by scanning electron microscope (SEM) images in Figure 6. Figure 6b and 6c show the images of the bump microcontact prior and after 60,000 cycles, respectively. The bottom contact pad after 60,000 cycles is seen in Figure 6d.

Other studies on thermomechanical failures such changes of the mechanical properties of contact material, the modifications of the contact topology and the diminution of the time dependence creep effect have been investigated for Au-to-Au microcontacts by [18].

2.5. Experimental limitations

The MEMS micro-fabrication techniques like the surface manufacturing and the bulk manufacturing do not guarantee uniform specimen dimensions. Cantilevers made by bulk manufacturing can result to dimensional deviations of 1 to 2 μm [19]. Thickness is particularly the major sources of error in the determination of the Young's modulus and yield strength. The dependency of the cantilever Young's modulus and the yield strength to the thickness third power and second power, respectively, can impair the measurements of the MEMS bending tests (equations 1 and 2). Furthermore, the measurement technique of the cantilever dimensions may also be an additional source of error. The dimensional variations may cause 13% deviation in the Young's modulus and 9% deviation in the yield strength [6].

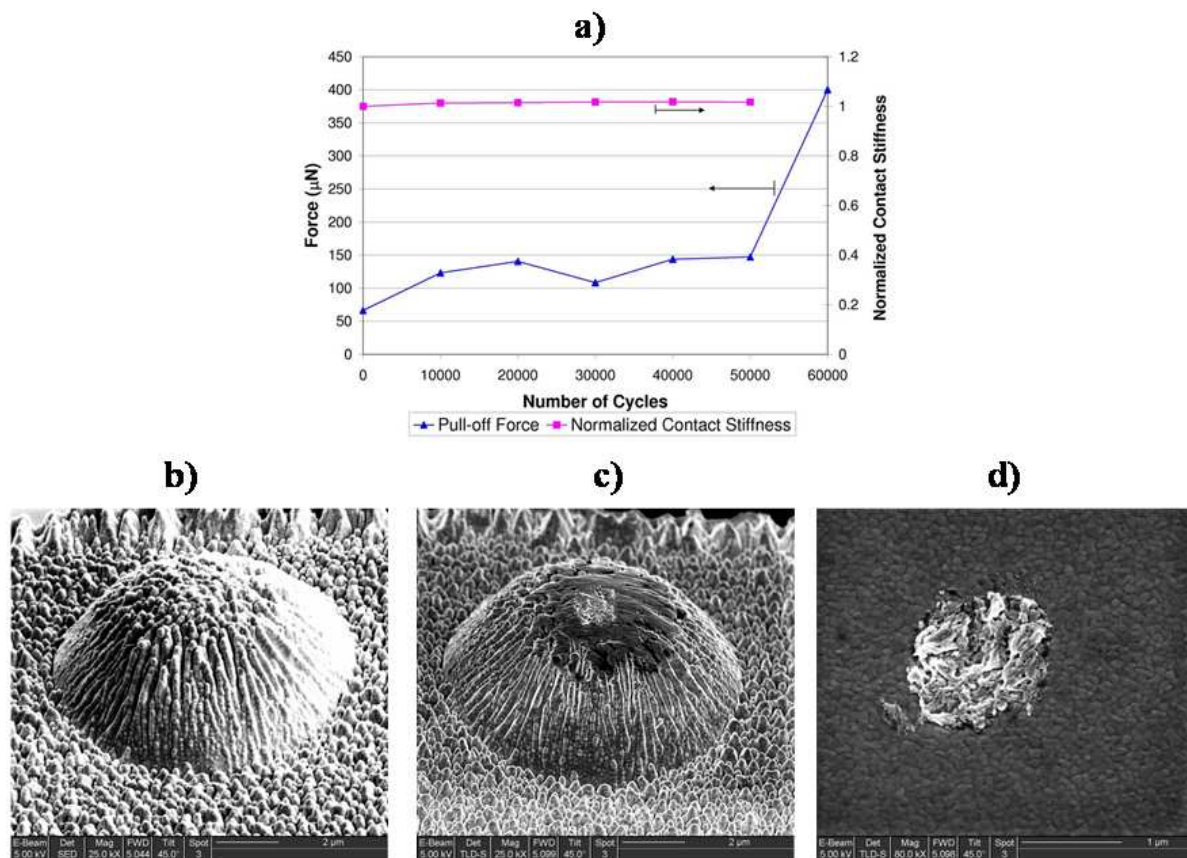


Figure 6. Images of microcontacts during cantilever tests a) gold contact bump prior cycling b) gold contact bump after 60,000 cycles and adhesive failure and c) bottom contact after 60,000 cycles adhesive failure [17].

To reduce the impact of cantilever dimensions on the mechanical properties, the use of focused ion beam (FIB) was suggested as a manufacturing technique since $0.03\mu\text{m}$ thickness variation was achieved for thin Al film ranged from 0.8 to $1.2\mu\text{m}$ [20].

Other aspects such as tip geometry and cantilever with strong texture must be considered during the MEMS bending test by nanoindentation. The standard Berkovich pyramidal tip can penetrate the cantilever material leading to an overestimation of the recorded deflection and therefore inaccurate mechanical properties based on equations 1 to 6. Removing the tip penetration from the recorded displacement or using blunt tip must be considered. However, in some cases, the tip penetration depth can be neglected when it is so much smaller than bending displacement. For highly anisotropic thin film such electroplated Cu which has strong texture, the corresponding Young's modulus is accordingly anisotropic. In this case, the measured Young's modulus of the cantilever by nanoindentation bending test represents the elastic modulus in parallel direction to the surface of Cu thin film which differs to the Young's modulus in the perpendicular direction [9].

3. Size effects study by uniaxial compression of micropillars

The nanoindentation technique can also be used to perform the uniaxial compression of micropillars for the purpose of investigating the influence of the size scale effects on the

plastic response of the material constituting the micropillars. The first work of the uniaxial compression of micropillars by nanoindentation was done by Uchic et al. [21]. Micropillars have diameter varying from hundreds of nanometers to tens of micrometers with an aspect ratio ranging from 2:1 to 4:1. Most of micropillars are fabricated using focused ion beam milling to create samples of uniform cross-section that remain attached to the bulk. Compression testing is carried out using a nanoindenter ended with a flat tip. The extracted load-displacement data are converted into stress-strain curves with the intention of investigating the plastic response of micropillar samples of different materials.

3.1. Size effects on plastic deformation

A size-scale effect can be defined as a change in material properties due to a variation in either the dimensions of an internal feature or structure or in the overall physical dimensions of a sample. When a crystal deforms plastically, phenomena such as dislocation storage, multiplication, motion, pinning, and nucleation are generally active over different length scales. So the understanding of the material deformation in micro or submicron scale is a main issue that allows designing reliable small devices [21].

An example of stress-strain curves of [111] Ni pillars with diameters ranging from 165 nm to 2 μm is presented in Figure 7 [22]. Two interesting observations can be found from the analysis of these curves. The first one is related to the evolution of the yield strength during compression as function of the micropillar diameters. At micron and submicron sizes, the yield strength, σ_y , was found to rise significantly when the micropillar diameter, d , decreases for various Ni and Ni alloy [21-23], Au micro/nano pillars [24,25], and Al [26] micropillars.

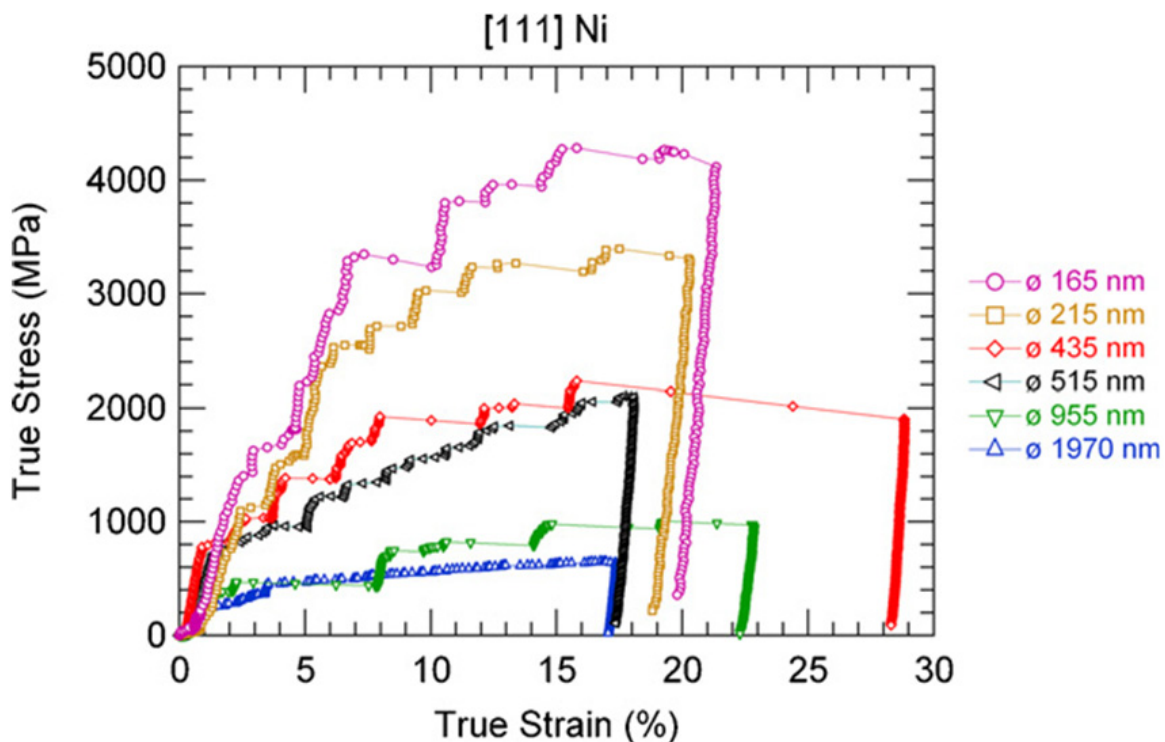


Figure 7. Stress-strain curves for [1 1 1] Ni pillars of various diameters [22].

The relationship between the two parameters can be expressed as follow:

$$\sigma_y \approx d^{-n} \quad (9)$$

Although the parameter n depends on the micropillar size and material as well as the compression strain of the micropillar under test, its value is comprised between 0.6 and 1 for all the studies reported in this work. As a result, the micron and submicron pillars yielded at stresses much higher than the typical yield strength of bulk materials where the yield strength, given by Hall-Petch relation, is proportional to the inverse square root of the average grain diameter. Furthermore, the size effect on the plastic yielding is insensitive to the micropillar fabrication method [24, 25].

The second observation seen from the compression of micropillars (Figure 7) is that all curves display during compression fast transients of strain, i.e., rapid bursts of strain separated by elastic loading segments. These bursts have been widely reported in several works [21-26].

The interpretation of the high flow stresses as well as the strain bursts of the micropillars under uniaxial compression remains an open question. One popular theory suggested a lack in dislocation multiplication events during deformation due to the small distances travelled by the dislocations before reaching the free surface of the micropillar. This leads to a dislocation free test structure and correspondingly a high flow stresses necessary to nucleate new dislocations and continue deformation. This theory is termed dislocation starvation theory [24, 25]. The dislocation starvation model was corroborated by the work in reference [26], where the authors investigated transmission electron microscopy (TEM) images of the dislocation structures which showed that the dislocation density of the micropillars did not grow significantly after severe deformations.

3.2. Experimental limitations

During nanoindentation tests, great efforts must be made to ensure that the measured deformation is due to the actual compression of the micropillars. To achieve this, firstly, the flat tip of the nanoindenter must be as parallel as possible to the top surface of the micropillar (perfect alignment); otherwise, the contact stiffness of the micropillar under test will be underestimating and as a result, the corresponding measured Young's modulus would be smaller than it should has been. In addition, severe misalignment will result in plastic buckling of the micropillars especially those with high aspect ratio. This will consequently affect the experimental stress-strain curves [27]. The misalignment between the flat tip and the micropillar top surface can be minimized by using a tiltable stage to hold the micropillar samples. Secondly, friction between the flat tip and the micropillar is also another issue and it may increase the yield strength, as well as prevent crystallographic rotation of the pillar during deformation [28]. However, some friction has been shown to be necessary to suppress plastic buckling of the sample [27]. Finally, another main concern that may have significant impact on the accuracy of the stress-strain curves is the actual

measurement of the deformation of the micropillars. Indeed, the nanoindenter is sensitive to any deformation of all the structures under test including the elastic deformation of the substrate where the micropillar is attached. Accurate determination of the true compression of the micropillar requires accounting for the elastic displacement, h_s , of the substrate under the micropillar which is calculated by using the Sneddon's solution of a cylindrical punch with diameter, d , pressed into an elastic half-space [29]:

$$h_s = \frac{1}{E_{eff}} \left(\frac{P}{d} \right) \quad (10)$$

P and E_{eff} are the applied load and the effective Young's modulus of the substrate material, respectively. The actual micropillar displacement, h , is deduced by subtracting the substrate displacement from the measured displacement, h_{meas} [22, 28]:

$$h = h_{meas} - \frac{1}{E_{eff}} \left(\frac{P}{d_b} \right) \quad (11)$$

where d_b represents the diameter of the micropillar base.

4. Analysis of cylindrical bump insertion using the nanoindentation technique for fine pitch interconnection applications

The insertion technology of cylindrical bumps was proposed as an alternative solution for ultra fine pitch flip-chip 3D interconnection technology in order to overcome process limitations caused by planarity defects, high process loads and temperature, or exhibit low hybridization speeds [30-33]. The insertion concept consists of the penetration of hard cylindrical bumps or microinserts into a softer thin film material in order to achieve mechanically and electrically reliable contacts. The insertion process allows finer pitch possibilities than the conventional flip chip because $2\mu\text{m}$ diameter microinserts have been achieved [31]. The standard flip chip and the insertion processes are illustrated in Figure 8a and 8b, respectively. Nanoindentation is used to clarify the contact formation mechanisms, the performance and the reliability during insertion. Unlike the previous sections, here the standard nanoindenter tip is replaced by a holder which receives the cylindrical bump sample. The study is focused on the insertion test of a single microinsert.

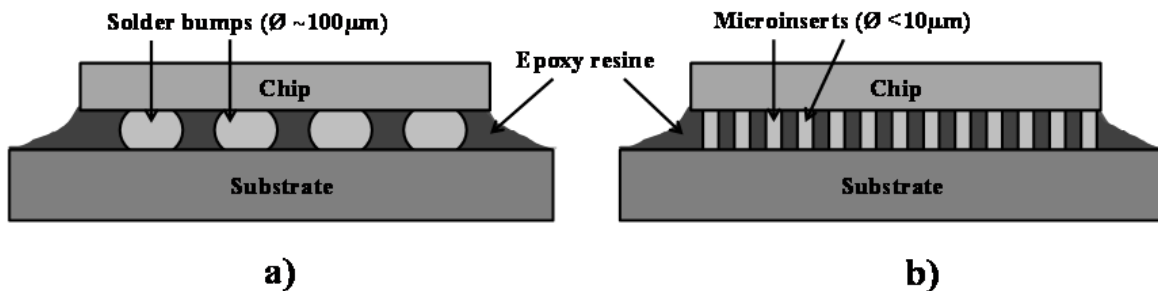


Figure 8. Schematic of flip chip interconnection technique a) Standard microbump and b) Insertion process.

4.1. Experimental details

4.1.1. Sample description

The microinsert used in this study is based on Ni material due its high hardness value and the thin film is made of Al which is a common layer of the substrate bond pad in flip chip technology. Therefore, two kinds of samples are fabricated. In both cases, Si wafer with 0.5 μm thick thermal oxide is used as starting substrate. The Ni microinsert is electroplated after photolithography steps on an Al sputtered thin film (1000 nm) covered by a Cu seed layer (500 nm). Experiments are performed with three nominal Ni microinsert diameters of 6 μm , 8.5 μm and 12.5 μm having the same height of 5 μm . The second test sample is a 450 nm Al thin film deposited on a 10 nm adhesion layer of W and a 250 nm diffusion barrier of WN. The two substrates are diced into 1.4 x1.4 mm² and 1x1 cm² chips for Ni microinsert and Al film samples, respectively.

4.1.2. Modified nanoindenter

For the experiments presented here, the standard nanoindenter tip is replaced by a holder which receives the Ni microinsert test sample. The second modification is related to the use of a $\pm 2^\circ$ tiltable stage to support the Al sample instead of the conventional substrate holder. To perform the electrical measurement during the insertion, Ni microinsert and Al samples are directly wire-bonded to contact pads integrated into the sample holders which are connected to a voltage/current sourcing and measurement unit. Figure 9 shows the modifications made in the nanoindenter for insertion tests. Four-point probing technique is used in order to eliminate resistance contribution of the wiring and the connections.

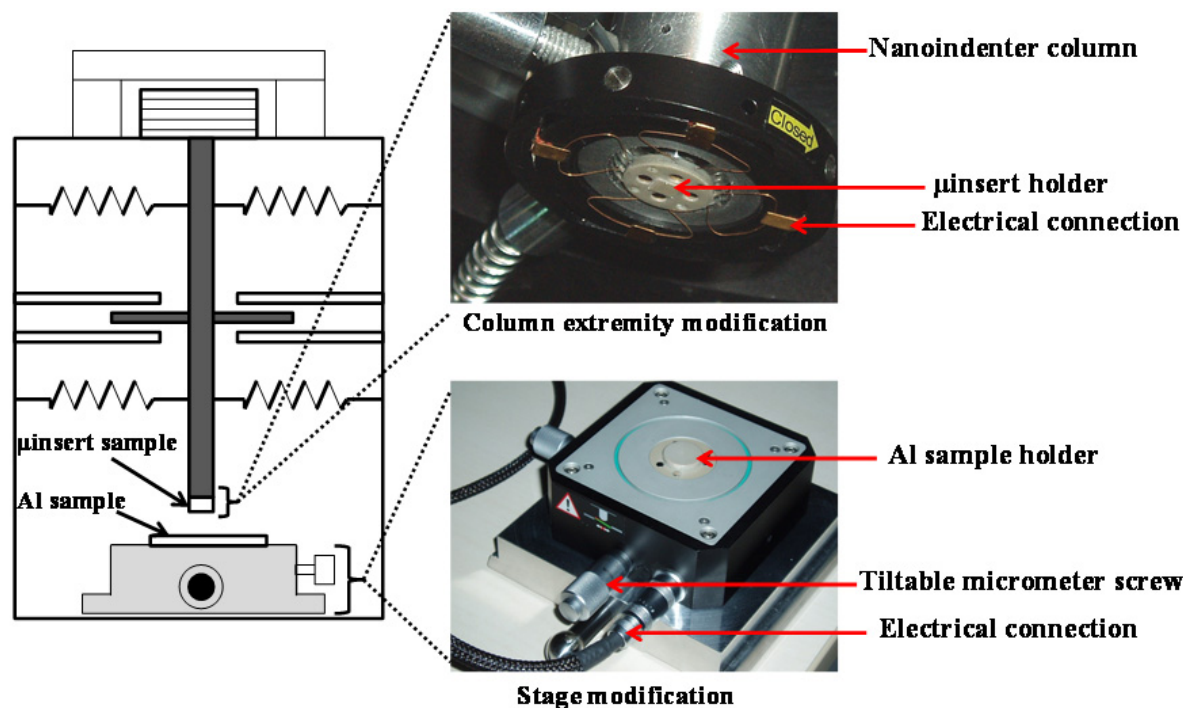


Figure 9. Principle of insertion test by modified nanoindentation.

4.1.3. Preliminary operations

The microinsert sample dimensions and the Ni and Al surfaces misalignment can be an obstacle to successfully performing insertion experiments. Hence, prior to experiments, we first carried out a mechanical polishing of Ni microinsert sample edges to avoid their contact with the target Al thin film. Then the sample misalignment with respect to the indentation axis is estimated by standard nanoindentation and correction is made. The misalignment of the Al surface can be reduced below 0.04° with the tiltable stage and the Ni microinsert sample misalignment is found to be less than 1° . Another operation which must be done before performing the experiments is the estimation of the additional frame compliance due to the Ni microinsert holder and the Al holder contributions. The new frame compliance is estimated using the Oliver and Pharr method [5] and its value is equal to 10^6 N/m which corresponds to a system less stiff than the classical nanoindentation frame ($\sim 8 \times 10^6$ N/m). This new compliance allows subtracting the displacement due to the deformation of the sample holders from the raw displacement data recorded during insertion.

These preliminary operations ensure that the displacement measurement is only related to the insertion of the Ni microinsert into the Al film.

4.1.4. Test procedure

The experiments are performed at room temperature with a single Ni microinsert. The insertion of Ni microinsert into Al film is made with a single loading/unloading cycle separated by a hold period of 600 secs at maximum load. This hold period is called first creep and it allows studying the creep phenomenon during insertion process. The unloading is stopped just before its end at low load for a second creep stage in order to follow an eventual deformation recovery. A thermal drift correction not described here was performed prior to the loading step. For each Ni microinsert diameter (6 μm , 8.5 μm and 12.5 μm), three maximum loads are applied corresponding to the equivalent uniaxial stresses of 0.8 GPa, 1.6 GPa and 3.2 GPa. Table 2 summarizes the experimental parameters.

Microinsert diameters	6 μm			8.5 μm			12.5 μm		
Maximum load (mN)	23	46	92	46	92	184	100	200	400
Uniaxial stress (GPa)	0.8	1.6	3.2	0.8	1.6	3.2	0.8	1.6	3.2
Loading time=Unloading time (sec)	0.5	1	2	0.5	1	2	0.5	1	2
1 st holding time = 2 nd holding time (sec)	600								

Table 2. Experimental parameters used for insertion tests.

4.2. Results and discussion

4.2.1. Mechanical behavior during insertion

The insertion curves (the plots of the load versus displacement) for each microinsert diameter at different maximum loads are presented in Figure 10, 11 and 12. It is important to point out that these curves represent the behavior of the global system in contact during the insertion test taking into account Al target film, Ni microinsert, the microinsert landing pad and the elastic deformation of both Si substrates. The goal of the authors was to use these curves to understanding the failure of the materials during the insertion for process validation; so less focus was dedicated to the mechanical parameters extraction. Only creep study was done and will be presented further.

According to diameters, the curves show similar evolution. So, for sake of simplicity, the results and analysis will be done only for 6 μm diameter microinsert. Sample characterizations with AFM, optical profiler and SEM are made on each Ni microinsert prior and after tests as well as the residual impression on Al thin film. Figure 13 shows the images of the 6 μm diameter microinserts with their corresponding residual impressions on Al films at the three maximum stresses.

Results from the three microinsert diameters show that the microinserts deform elastically for the applied maximum stresses of 0.8 GPa and 1.6 GPa, while at 3.2 GPa, a large plastic compression is noticed. A penetration of the microinserts into their landing pad which is constituted of Cu(500nm)/Al(1000 nm) layers is observed at 1.6 GPa and 3.2 GPa (Figure 13a(2) and 13a(3)). This is confirmed by the presence of pile-up around the microinsert base. The combination of the large plastic compression of the microinserts and the penetration into their landing pad, produce a large deformation that corresponds to an abrupt slope change of the insertion curves at applied maximum stress of 3.2 GPa (see Figure 10, 11 and 12). For Al thin film, the deformation is elastic-plastic and the insertion height increases with the maximum applied stresses for all microinsert diameters. At 0.8 GPa, the residual impression is superficial and is due to the roughness of the microinsert surface. At 1.6 GPa and 3.2 GPa, the average insertion heights are 60 nm and 280 nm, respectively. These values are lower than the penetration depths of the microinserts into their landing pad which are 260 nm and 710 nm at 1.6 GPa and 3.2 GPa, respectively. So, the microinserts penetrate mostly into their landing pad rather than into the facing thin Al film.

4.2.2. Al creep parameters

The creep parameters of the thin Al film were extracted from the insertion curves in Figure 10, 11 and 12. It was necessary to deduce from these curves the only displacement which occurs within the Al film since displacement measured during the first creep stage takes into account the displacement of the whole system. To achieve this goal, insertion tests with the experimental parameters presented in table 2 were reproduced by replacing the Al film by a Si substrate. As the deformation within Si substrate is perfectly elastic during the contact with Ni microinsert, Al creep curves are obtained by subtracting the creep curves of Ni/Si contact from the creep curves of Ni/Al contact. This approach was found to be correct only

with 12.5 μm diameter Ni inserts. For smaller diameter, Ni deformation at Si contact was not similar to Ni deformation at Al contact and results could not be used confidently.

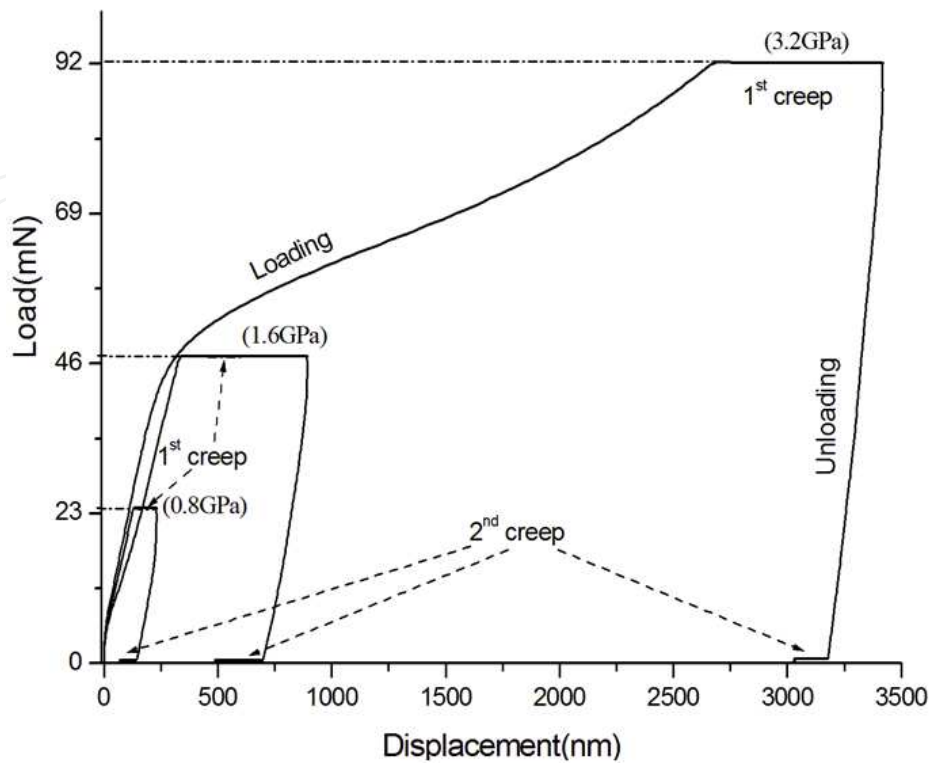


Figure 10. Insertion curve of 6 μm Ni diameter at different maximum loads.

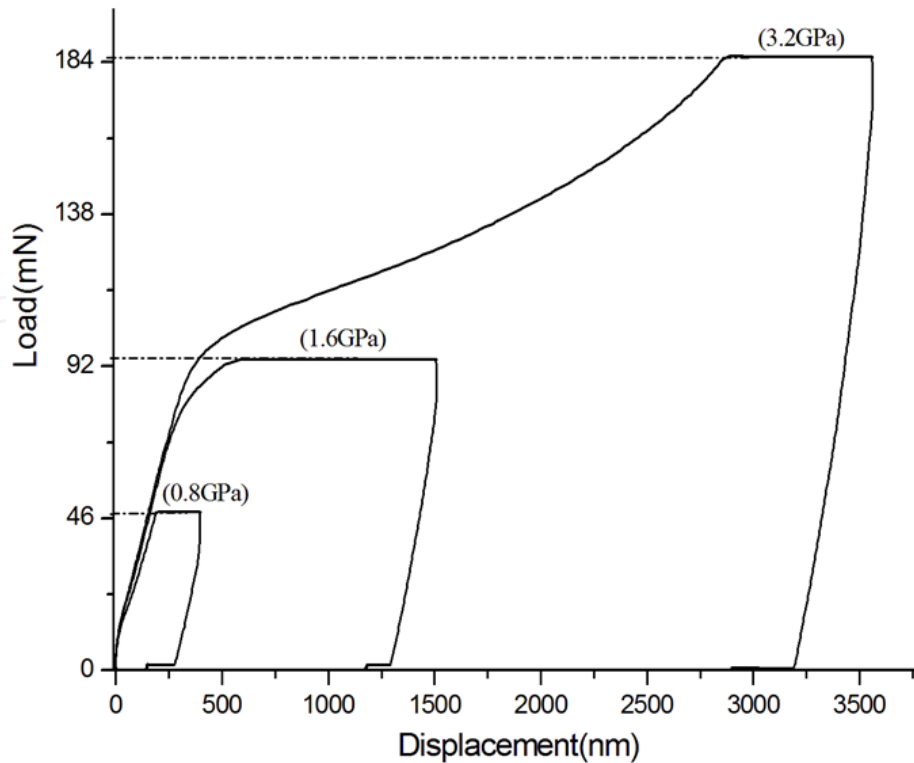


Figure 11. Insertion curve of 8.5 μm Ni diameter at different maximum loads

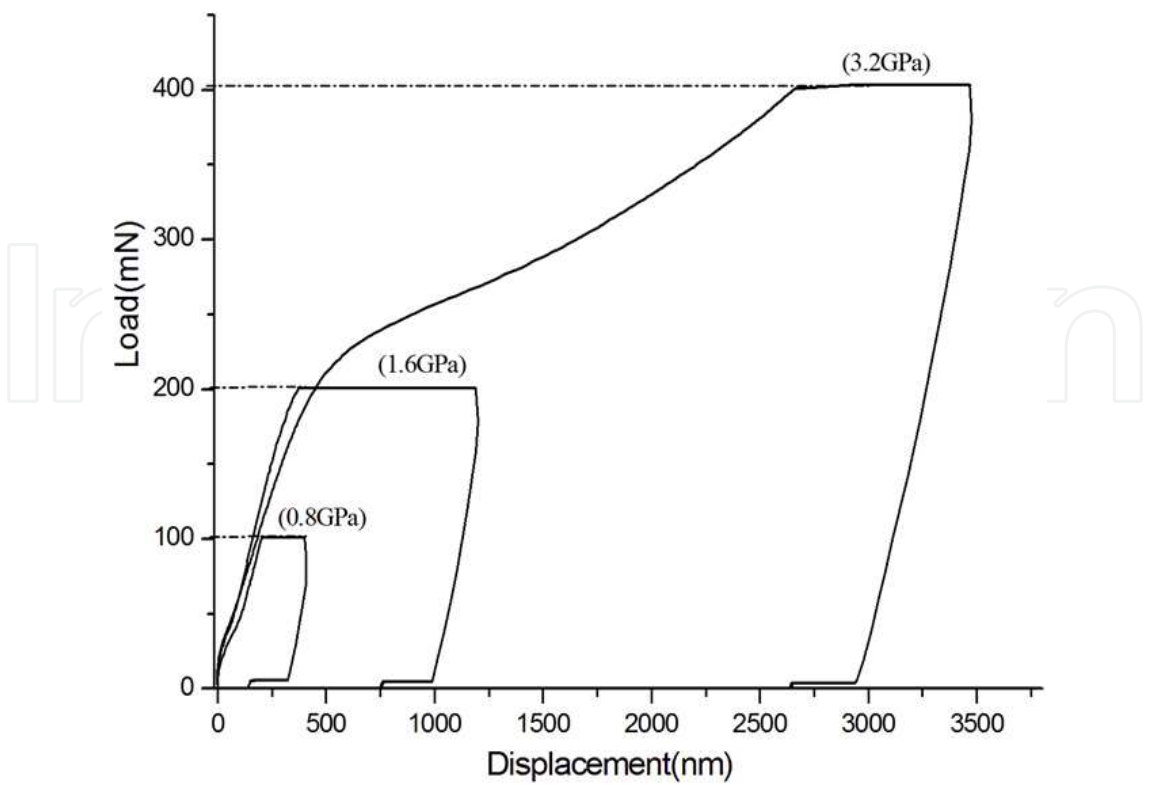


Figure 12. Insertion curve of 12.5 μm Ni diameter at different maximum loads.

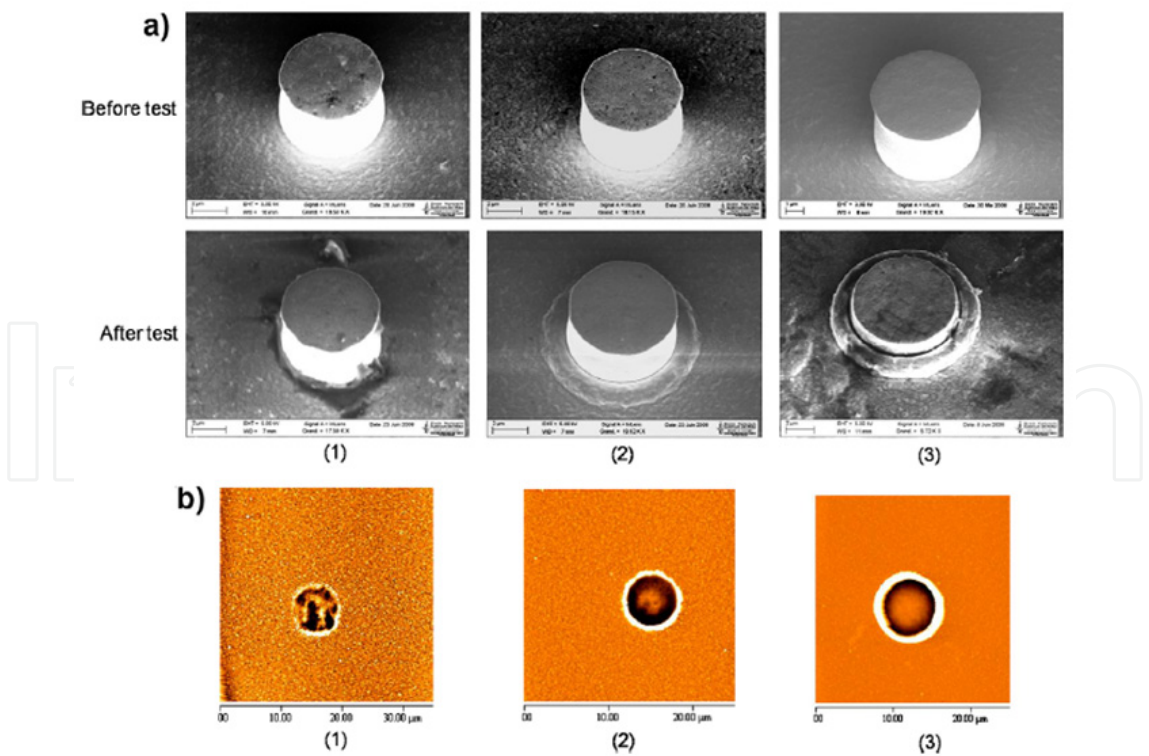


Figure 13. Samples characterization of insertion tests with 6 μm diameter Ni microinserts (a) microinserts before and after tests and (b) residual impression on Al film after test. (1–3) referred to maximum load of 23 mN (0.8 GPa), 46 mN (1.6 GPa) and 92 mN (3.2 GPa), respectively.

Figure 14 presents Al creep curves obtained after insertion with 12.5 μm diameter Ni microinsert for the first creep stages. Primary or delayed creep followed by secondary or steady creep is observed. One can notice a larger displacement variation of the curve obtained with a load of 200 mN compared to the one obtained with 400 mN. An explanation could be related to the fact that at 400 mN the microinsert showed a large plastic deformation prior the creep stage. This result to a larger contact area and a significant influence of the presence of the Si substrate underneath the Al film which both limit the creep deformation.

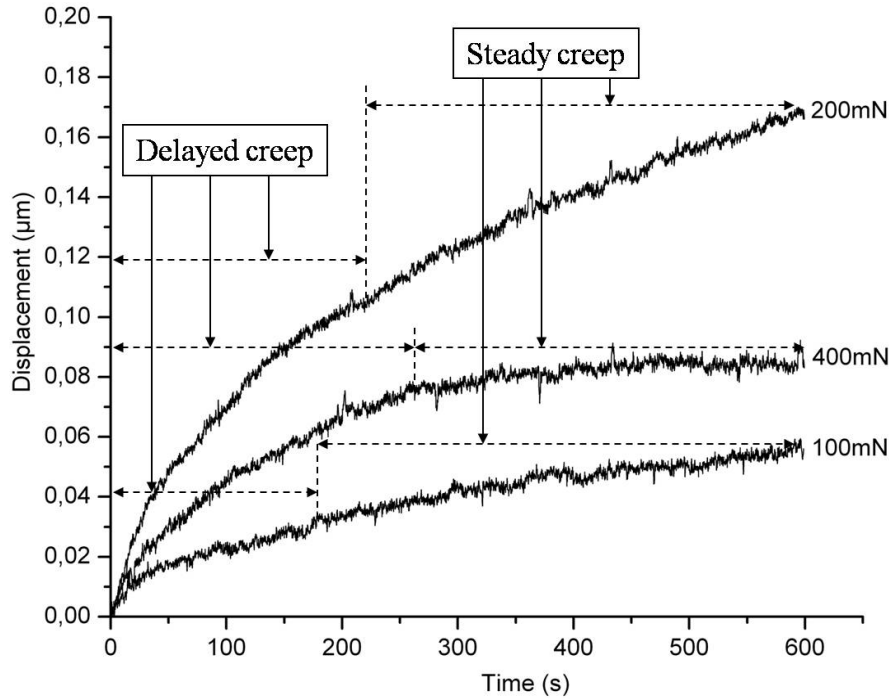


Figure 14. Al creep curves with 12.5 μm Ni microinsert at maximum loads of 100mN, 200mN and 400mN.

To extract Al creep parameters, a Maxwell/Kelvin-Voigt phenomenological model was used. In the case of a Ni microinsert with a radius r inserted into Al, displacement change is given as function of time under a constant load P by:

$$h(t) = \frac{P}{r} \left[\frac{1}{E_1} + \frac{1}{E_2} \left(1 - e^{-\frac{tE_2}{\eta_2}} \right) + \frac{1}{\eta_1} t \right] \quad (12)$$

where E and η are phenomenological parameters related to the spring and the dashpot viscosity coefficient of the model, respectively. The indexes (1) and (2) refer to Maxwell element and Voigt-Kelvin element, respectively. The equation (12) is fitted to the experimental Al creep curves for parameter extraction. The $1/E_1$ term corresponds to Al young modulus and it is not included in the creep curves; so the extracted parameters here are E_2 , η_1 and η_2 (Table 3).

Creep load (mN)	100	200	400
E_2 (GPa)	637	412	614
η_1 (GPa s)	$3 \cdot 10^5$	$2 \cdot 10^5$	$6 \cdot 10^{28}$
η_2 (GPa s)	$5 \cdot 10^4$	$3 \cdot 10^4$	$8 \cdot 10^4$

Table 3. Al creep parameters after insertion with 12.5μm Ni microinsert at different maximum loads

Creep at maximum loads reveals a weak variation of parameters as function of load except the value of η_1 for a 400mN load which tends towards infinity. This could be explained by the large contact area and the influence of the Si substrate resulting from the large plastic deformation prior the creep stage.

The creep parameters extracted here can be helpful for insertion process analysis and prediction.

4.2.3. Materials optimization and electrical resistance results

The results presented in section 3.1.1 reveal the mechanical failures of the material layers underneath the microinserts at certain stresses as well as the insufficient penetration of the microinsert into the facing Al film. Design optimization of the microinserts as well as material and thickness selections of the microinsert landing pad are required to achieve reliable insertion interconnection technology. Thus, a microinsert based on microtube geometry with 10μm pitch has been proposed by [30, 33] in order to reduce the cross sectional area of the microinsert, hence the assembly insertion load. These works have demonstrated higher insertion penetration of microtubes of different materials and dimensions into a thicker film compared to the 450 nm Al film used in section 3.2.1. In addition, since the lateral contact surface increases during the microtube insertion, the corresponded resistance is lower than the measured resistance of the insertion of Ni cylindrical bumps. Figure 15 shows the evolution of the insertion and resistance curves versus time of the two microinsert geometries. The Figure 15a and 15b do not have similar test parameters. On the one hand Figure 15a was extracted by applying a load (92 mN, 300 secs)/unload (300 secs) cycle without any holding stage; on the other hand, Figure 15b was obtained with a faster loading rate (300 μN/sec) at a maximum load below 9 mN. Another noticed difference is that the displacement presented in Figure 15a also takes into account the plastic deformation of the microinsert and its landing pad while the Figure 15b was based exclusively on the insertion of the microtube. Despite this difference in testing conditions, one can find that the interconnection resistance was less than 4 Ω in less than 10 seconds and a maximum insertion higher than 1.6 μm was achieved with the microtube insertion (see Figure 15b). Unlike the insertion of the standard microinsert (see Figure 15a) where a stable resistance of 20 Ω was measured and the maximum insertion was 224 nm. Besides the lateral contact surface, a 240 nm gold layer deposited onto the microtubes greatly influences the lower resistance during microtube insertion.

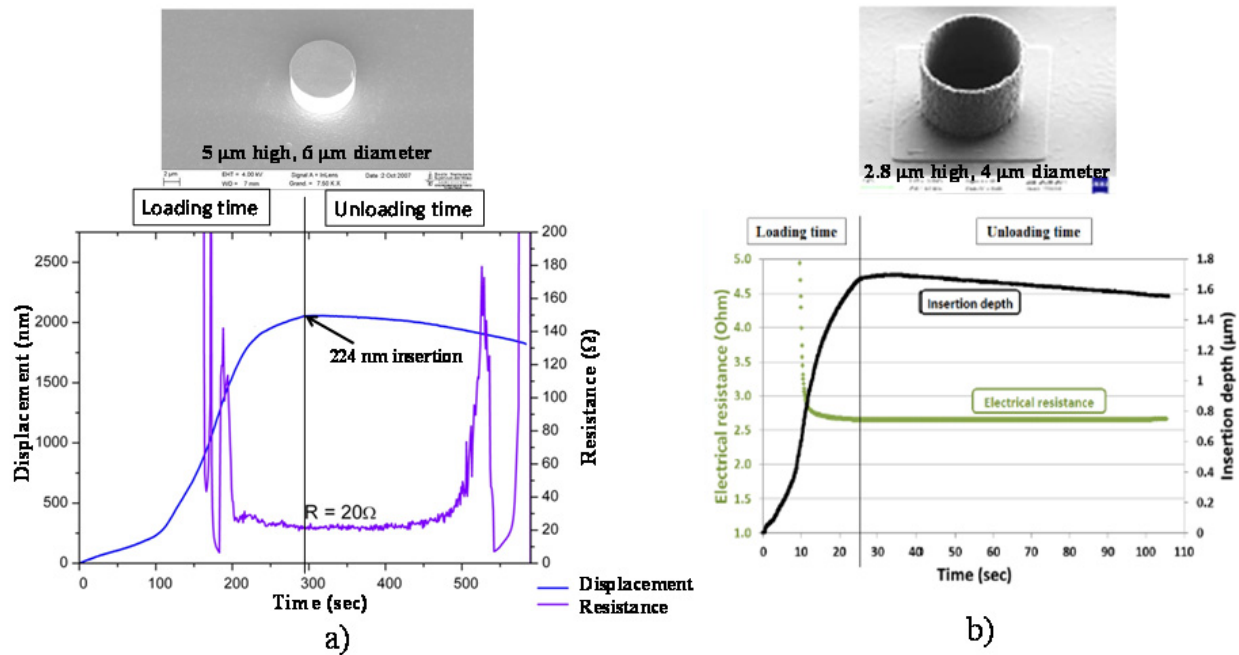


Figure 15. Insertion and resistance measurements versus time a) $6\ \mu\text{m}$ diameter microinsert and b) $4\ \mu\text{m}$ diameter microtube [32, 33].

The results extracted from the single microtube were used for process parameters to carry out reliable Die To Wafer (D2W) integrations taking into account industrial requirements. The Figure 16 illustrates 183 D2W integrations carried out on a 200 mm wafer; each chip that has about 95,000 interconnections was assembled using the results of single microtube insertions [33].

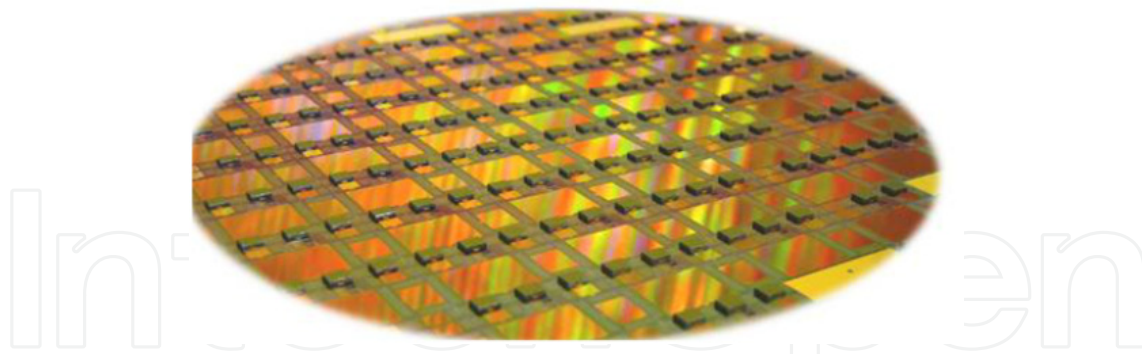


Figure 16. Populated 200mm wafer with different insertion conditions for process validation. [33].

5. Conclusion

The use of the nanoindentation technique beyond continuous thin films characterization offers many possibilities for evaluating materials properties such as elastic-plastic constants and fatigue strength at micrometer and submicrometer scales of patterned structures. The experimental data are essential not only in materials selection and designing structures, but also for ensuring the reliability during operation of the microdevices. The research potential of the nanoindentation should be considered beyond the case studies presented here. As an

example, carbon nanotubes (CNTs) mechanical characterization by nanoindentation is another attractive subject since few experimental results exist despite its fundamental importance and applications. Whatever the samples under test is and whatever the modifications on nanoindentation tool are, a particular attention should be paid on the extracting data by ensuring that they reflect the deformation of the structures under test. However, nanoindentation tests suffer from low accuracy in displacement at high temperature loading despite recent development made in this area. Another limitations also encountered in continuous thin films tests is the difficulty to dissociate thin film characteristics from the underlying layers or substrate contributions. Overcoming these limitations can be made through theoretical models and finite element simulations. As the need for accurate reliability data on materials used in microdevices expands, so will characterization techniques such as nanoindentation.

Author details

Mamadou Diobet DIOP

*Faculty of Engineering, Department of Electrical and Computer Engineering,
University of Sherbrooke, Sherbrooke, Quebec, Canada*

6. References

- [1] Fischer-Cripps AC. Introduction to Contact Mechanics. Mechanical Engineering Series, Springer-Verlag New York, Inc.; 2000.
- [2] Tabata O., Tsuchiya T. Reliability of MEMS: Testing of materials and devices. Advanced Micro & Nanosystems. Volume 6. WILEY-VCH Verlag. Weinheim, Germany; 2008.
- [3] Shen YL. Constrained Deformation of Materials Devices. Heterogeneous Structures and Thermo-Mechanical Modeling. Springer Sciences, New York; 2010.
- [4] Tummala RR. Fundamentals of Microsystems packaging. McGraw-Hill; 2001.
- [5] Oliver WC., Pharr GM. Measurement of hardness and elastic modulus by instrumented indentation: Advances in understanding and refinements to methodology. Journal of Materials Research 2004; 19(1) 3-20.
- [6] Bravman JC., Weihs TP., Hong S. Nix WD. Mechanical deflection of cantilever microbeams: A new technique for testing the mechanical properties of thin films. Journal of Materials Research 1988; 3(5) 931-942.
- [7] Timoshenko SP., Gere JM. Mechanics of Materials. Van Nostrand, New York; 1972.
- [8] Jeong JH., Son D, Kwon D. Film-thickness considerations in microcantilever-beam test in measuring mechanical properties of metal thin film. Thin solid Films 2003; 437(1) 182-187.
- [9] Hong SH., Kim KS., Kim YM, Hahn JH., Lee CS., Park JH. Characterization of elastic moduli of cu thin films using nanoindentation technique. Composites Science and Technology 2005; 65(9) 1401-1408.
- [10] Bhushan B. Nanotribology and Nanomechanics: An Introduction. 2nd edition, Springer-Verlag Heidelberg, Berlin; 2008.

- [11] Li X., Bhushan B. Fatigue studies of nanoscale structures for MEMS/NEMS applications using nanoindentation techniques. *Surface and Coatings Technology* 2003; 163 521–526.
- [12] Acar C., Shkel A. MEMS Vibratory Gyroscopes Structural Approaches to Improve Robustness. Springer publisher, New York; 2009.
- [13] Douglass MR. Lifetime Estimates and Unique Failure Mechanisms of the Digital Micromirror Device (DMD): proceedings of 36th IEEE International Symposium on Reliability Physics, March 31–April 2, 1998, Reno, Nevada, USA.
- [14] Majumder S., McGruer NE., Adams GG. Contact Resistance and Adhesion in a MEMS Microswitch: proceedings of the ASME/STLE International Joint Tribology Conference, 26–29 October 2003, Florida, USA.
- [15] Segueineau C., Broue A., Dhennin J., Desmarres JM., Pothier A., Lafontan X., Ignat M. MEMS Characterization – A new experimental approach for measuring electrical contact resistance by using nanoindentation: proceeding of 18th Workshop on MicroMechanics Europe, 16–18 Sept 2007, Guimarães, Portugal.
- [16] Holm H. Electrical contacts, Theory and applications. 4th ed., Springer-Verlag, Berlin; 1967.
- [17] Gilbert KW., Mall S., Leedy KD., Crawford B. A Nanoindenter Based Method for Studying MEMS Contact Switch Microcontacts: proceedings of the 54th IEEE Holm Conference on Electrical Contacts, 27–29 October 2008, Florida, USA.
- [18] Broue A., Dhennin J., Segueineau C., Lafontan X., Dieppedale C., Desmarres JM., Pons P, Plana R. Methodology to Analyze Failure Mechanisms of Ohmic Contacts on MEMS Switches: proceedings of the IEEE International Symposium on Reliability Physics, 26–30 April 2009, Montreal, Quebec, Canada.
- [19] Liu HK., Pan CH., Liu PP. Dimension effect on mechanical behavior of silicon micro-cantilever beams. *Measurement* 2008; 41(8) 885–895.
- [20] McCarthy J., Pei Z., Becker M., Atteridge D. Fib micromachined submicron thickness cantilevers for the study of thin film properties. *Thin solid Films* 2000; 358(1) 146–151.
- [21] Uchic MD., Dimiduk DM., Florando JM., Nix WD. Sample dimensions influence strength and crystal plasticity. *Science* 2004; 305(5686) 986–989.
- [22] Frick CP., Clark BG., Orso S., Schneider AS., Arzt E. Size effect on strength and strain hardening of small-scale [111] nickel compression pillars. *Materials science and engineering A* 2008; 489(1–2) 319–329.
- [23] Uchic MD., Dimiduk DM., Parthasarathy TA. Size-affected single-slip behavior of pure nickel microcrystals. *Acta Materialia* 2005; 53(15) 4065–4077.
- [24] Oliver WC, Greer JR., Nix WD. Size dependence of mechanical properties of gold at the micron scale in the absence of strain gradients. *Acta Materialia*, 2005; 53(6) 1821–1830.
- [25] Greer JR., Nix WD. Nanoscale gold pillars strengthened through dislocation starvation. *Physical Review B* 2006; 73(24) 245410.
- [26] Ng KS., Ngan AHW. Stochastic nature of plasticity of aluminum micro-pillars. *Acta Materialia* 2008; 56(8) 1712–1720.
- [27] Wei Q., Zhang H., Schuster BE., Ramesh KT. The design of accurate micro-compression experiments. *Scripta materialia* 2006; 54(2) 181–186.

- [28] Orso S., Frick CP., Arzt E. Loss of pseudoelasticity in nickel-titanium sub-micron compression pillars. *Acta Materialia* 2007; 55(11) 3845-3855.
- [29] Sneddon IN. The relation between load and penetration in the axisymmetric boussinesq problem for a punch of arbitrary profile. *International Journal of Engineering Science* 1965; 3(1) 47-57.
- [30] Saint-Patrice D, Marion F., Fendler M., Dumont G., Garrione J., Mandrillon V., Greco F., Diop M., Largeron C., Ribot H. New Reflow Soldering and Tip in Buried Box (TB2) Techniques For Ultrafine Pitch Megapixels Imaging Array: proceedings of the 58th Electronic Components and Technology Conference, 27-30 May 2008, Orlando, Florida, USA.
- [31] Boutry H., Brun J., Franiatte R., Nowodzinski A., Sillon N., Dubois-Bonvalot B., Depoutot F., Brunet O., Peytavy A. Reliability characterization of Ni-based microinsert interconnections for flip chip die on wafer attachment and their evaluation in multichip simcard prototype: proceedings of the 10th IEEE Electronics Packaging Technology Conference, 9-2 December 2008, Singapore.
- [32] Diop MD., Mandrillon V., Boutry H., Fortunier R., Inal K. Analysis of nickel cylindrical bump insertion into aluminium thin film for flip chip applications. *Microelectronic Engineering* 2010; 87(3) 522-526.
- [33] Goubault de Brugière B., Marion F., Fendler M., Mandrillon V., Hazotte A., Volpert M., Ribot H. A 10 μ m Pitch Interconnection Technology using Micro Tube Insertion into Al-Cu for 3D Applications: proceedings of the 61st IEEE Electronic Components and Technology Conference, 31 May – 3 June 2011, Lake Buena Vista, Florida, USA.